



City Research Online

City, University of London Institutional Repository

Citation: Chatterjee, S., Phillips, J. P. & Kyriacou, P. A. (2016). Monte Carlo investigation of the effect of blood volume and oxygen saturation on optical path in reflectance pulse oximetry. *Biomedical Physics and Engineering Express*, 2(6), 065018. doi: 10.1088/2057-1976/2/6/065018

This is the accepted version of the paper.

This version of the publication may differ from the final published version.

Permanent repository link: <https://openaccess.city.ac.uk/id/eprint/19813/>

Link to published version: <https://doi.org/10.1088/2057-1976/2/6/065018>

Copyright: City Research Online aims to make research outputs of City, University of London available to a wider audience. Copyright and Moral Rights remain with the author(s) and/or copyright holders. URLs from City Research Online may be freely distributed and linked to.

Reuse: Copies of full items can be used for personal research or study, educational, or not-for-profit purposes without prior permission or charge. Provided that the authors, title and full bibliographic details are credited, a hyperlink and/or URL is given for the original metadata page and the content is not changed in any way.

City Research Online:

<http://openaccess.city.ac.uk/>

publications@city.ac.uk

Monte Carlo investigation of the effect of blood volume and oxygen saturation on optical path in reflectance pulse oximetry

S Chatterjee, J P Phillips, and P A Kyriacou

Research Centre for Biomedical Engineering, City, University of London, Northampton Square, London EC1V 0HB, United Kingdom

Email: subhasri.chatterjee.1@city.ac.uk

Key words: Pulse oximetry, Monte Carlo, light tissue interaction, clinical applications

Abstract: Despite the clinical importance of pulse oximetry, the precise nature of the interaction of light with tissue, which underlies the technique, is not yet fully understood. The limitations of the method with regard to its accuracy in conditions of compromised perfusion and/or low blood oxygen saturations are well documented but have only partly been resolved. Results from a static monolayer Monte Carlo model of optical path and reflectance at two wavelengths most commonly used in pulse-oximetry (660 nm and 940 nm) through skin tissue, containing different volume fractions of blood with a range of oxygen saturations, are presented. Results exhibited differences in mean optical path between the two wavelengths, with differences generally increasing with increasing tissue oxygen saturation and decreasing blood volume. As an example, in a typical sensor configuration, the mean optical path of red light traveling through skin containing 7.5% blood volume fraction with mean oxygen saturation of 60% was 58% higher than that for infrared. The results presented should contribute to further understanding of the effect of physiological conditions such as anemia, ischemia and hypoxemia on the accuracy of pulse oximetry readings.

1. Introduction

Pulse oximetry is arguably the most significant technological development in patient monitoring in the last half century [1,2] and has become a standard of care in anesthesia and related medical specialties. Pulse oximetry is a non-invasive photometric method for estimation of arterial oxygen saturation from photoplethysmographic (PPG) signals [3]. The technique uses arterial pulsatility to discriminate between the absorption of light by arterial blood, known as the 'AC' component of the PPG, and other absorbers such as melanin, venous and capillary blood and other tissue, which contribute to the 'DC' component. The oxygen saturation is derived from the relative modulation of amplitude of red and near infrared light by the two common functional hemoglobins, namely, oxy- and deoxy-hemoglobin (HbO_2 and Hb respectively) in arterial blood to establish the relative abundance of each hemoglobin type [3].

A significant amount of work has been carried out in recent years mainly contributing to technological advancements of pulse oximeters [4-6], for example, to improve the signal quality and reduce artifact, particularly in states of motion or reduced perfusion. Furthermore, theoretical and numerical models [7-9] have been developed to explain the functionality of pulse oximeters. An experimental model using tissue phantoms has also been developed [10] to analyze the working principle of pulse oximetry. Moreover, basic pulse oximetry models of the light-tissue interaction and arterial mechanics have been challenged by recent research in this field [11-13]. However, some problems still remain. Available models for pulse oximetry do not explicitly describe the optical path of photons traveling through the tissue; nor do any of the models account for differences in the optical path for two (or more) different wavelengths. Also, the effects of changes in differential optical path caused by desaturation of *all* blood in tissue (i.e., arterial, capillary and venous) have never been investigated using any model. Similarly, no detailed consideration of differences in red and infrared optical paths induced by changes in tissue blood volume (i.e., the fraction of tissue volume occupied by blood) due to vasoconstriction or vasodilation is found in the literature.

A detailed knowledge regarding the optical path is desirable in order to optimize the positioning and geometry of pulse oximetry probes and gain understanding of the volume of tissue ‘interrogated’ by the probe. This knowledge also contributes to development of robust algorithms that provide accurate and precise readings over a range of physiological states. Additionally, such a study is crucial to overcome one of the main limitations of pulse oximetry, and one that is well known to experienced users, that is, its inaccuracy in poorly oxygenated patients. This is generally attributed to the lack of calibration data at arterial saturations less than 70% due to ethical constraints in obtaining such data in humans. However, the mechanism underlying the inaccuracy remains to be fully elucidated.

To address these questions, a static single layer Monte Carlo model was used to investigate the dependence of optical path on blood volume and blood oxygen saturation in a tissue with the optical properties of skin (dermis) containing blood. The Monte Carlo method is a well-known technique for solving problems related to light-tissue interaction that are too complex to solve analytically [14-16]. Using this method, a fiber-optic reflectance pulse oximetry probe was simulated, emitting two commonly used optical wavelengths for pulse-oximetry, 660 and 940 nm, onto skin dermis tissue. Although a non-pulsatile single layer model was used for the simulation, this served the main purpose of the paper, i.e., demonstrating variations of optical path through tissue under varying hemodynamic conditions encountered in pulse oximetry.

2. Methodology

2.1 Monte Carlo method

In a typical Monte Carlo optical model, virtual photon packets are simulated as they pass through a volume of tissue which is, in general, a highly scattering and partly absorbing medium with known optical properties. These properties are defined as the scattering coefficient μ_s , absorption coefficient μ_a and scattering anisotropy g , each being dependent on the photon wavelength λ . The steps of the general Monte Carlo method for light-tissue interaction have been explicitly described elsewhere [15,17].

In the present work, a Monte Carlo (MC) algorithm for light transport through a homogeneous layer of perfused tissue in a reflectance mode pulse oximetry set-up was implemented. The geometry of the three dimensional model is shown in figure 1.

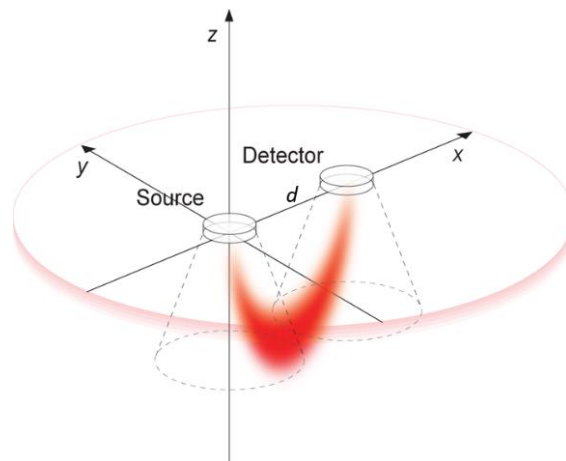


Figure 1. Geometry for Monte Carlo model in a reflectance pulse oximetry set-up, presented in Cartesian co-ordinates (x,y,z) . Circular source and detector are placed on x -axis at a distance d . Light is emitted from the source within a cone-shaped boundary (‘cone of emittance’, shown by dotted lines) and enters the detector if it falls within its ‘cone of acceptance’. The red banana shaped region is the expected path of the majority of light travelling from source to detector.

For simplicity and assuming the tissue dimensions to be much larger than the spatial extent of the photon distribution, the tissue layer was considered semi-infinite. As shown in figure 1, the tissue surface was represented by the x - y plane of the co-ordinate system. The fiber optic source was supposed to be placed at the origin of the system. The fiber optic detector was placed at a center-to-center distance d from the source along the x -axis, allowing the source-detector separation d to be varied for different simulation runs. The photons were launched from randomly chosen points in the circular emitter of radius r_s with a randomly generated angle within the numerical aperture (NA , the sine of the acceptance angle) of the source fiber. The distribution of the angle of emittance of the photons within the NA was considered to be uniform [19]. An initial statistical ‘weight’ $w=1$ was assigned to each photon packet. The optical path of the photon packet was simulated by tracing photon’s steps through the medium, determined by random sampling of the probability distribution for the photon’s free pathlength [18]. After propagating through tissue, if the photon packet was exiting the tissue surface ($z > 0$), a check was made to ensure whether the photon packet had fulfilled the detection criteria, i.e., it had reached within the area of the circular detector of radius r_d with an angle within the NA of the detector fiber. The history of the photon exiting the tissue without being detected was discarded. Russian roulette technique was used for termination of the photon packets within medium, weighing below the threshold weight ($w_{th} = 10^{-4}$) [17].

2.2 Optical properties

The perfused tissue layer used in the model was assumed to be a homogeneous mixture of skin-dermis and blood (comprising both oxyhemoglobin and deoxyhemoglobin) and was characterized by their optical properties. Considering tissue-homogeneity, the total absorption coefficient μ_a of a layer of skin dermis perfused with a volume fraction of blood V having a total oxygen saturation StO_2 may be written as the sum of the individual absorption coefficients of the components [7,20,21]:

$$\mu_a = (1-V)\mu_{a_{dermis}} + V \left[StO_2 \mu_{a_{blood_{100\%}}} + (1-StO_2)\mu_{a_{blood_{0\%}}} \right] \quad (1)$$

where $\mu_{a_{dermis}}$ is the absorption coefficient of skin-dermis tissue, $\mu_{a_{blood_{100\%}}}$ and $\mu_{a_{blood_{0\%}}}$ are the absorption coefficients of oxygenated (oxygen saturation $\approx 100\%$) and deoxygenated (oxygen saturation $\approx 0\%$) blood respectively. The total oxygen saturation StO_2 is given by,

$$StO_2 = \frac{[HbO_2]}{[HbO_2] + [Hb]} \quad (2)$$

where $[HbO_2]$ and $[Hb]$ are the concentrations of oxyhemoglobin and deoxyhemoglobin respectively in the total blood volume, i.e., the all blood found in the arterial, capillary and venous compartments.

Again, considering the ideal tissue-homogeneity, the total reduced scattering coefficient μ'_s [where $\mu'_s = \mu_s(1-g)$] also may be written as:

$$\mu'_s = (1-V)\mu'_{s_{dermis}} + V \left[StO_2 \mu'_{s_{blood_{100\%}}} + (1-StO_2)\mu'_{s_{blood_{0\%}}} \right] \quad (3)$$

$\mu'_{s_{blood_{100\%}}}$ and $\mu'_{s_{blood_{0\%}}}$ being the reduced scattering coefficients of oxygenated and deoxygenated blood respectively. The absorption coefficient of bloodless skin dermis at any wavelength was approximated from the following equation, based on measurements from rat skin samples, which are optically quite similar to neonatal skin [21]:

$$\mu_{a_{dermis}}(\lambda) = 0.0244 + 8.53e^{-\frac{\lambda-154}{66.2}} \left(mm^{-1} \right) \quad (4)$$

The reduced scattering coefficient of bloodless dermis was estimated from the contribution of dermis collagen fibers, primarily, to Mie and Rayleigh scattering, as shown in Eq. 5 [21]:

$$\mu'_{s_{dermis}}(\lambda) = \left(2 \times 10^4 \right) \lambda^{-1.5} + \left(2 \times 10^{11} \right) \lambda^{-4} \left(mm^{-1} \right) \quad (5)$$

Calculated values from above equations at 660 nm and 940 nm were in good agreement with the published values of optical properties of human (Caucasian) dermis [22]. The calculated values of $\mu_{a_{dermis}}$ and $\mu'_{s_{dermis}}$ at 660 nm and 940 nm used for present model are given in Table 1. The optical properties of oxygenated and deoxygenated blood having hematocrit (Hct, proportion of red blood cells in total blood volume) 45% were collected from published literature [23,24]. The absorption and reduced scattering coefficients of blood at 660 nm and 940 nm, used in the model, are given in Table 1. The anisotropy factor value for the perfused skin tissue layer was taken to be $g = 0.95$ at both wavelengths and the refractive index of the tissue layer was considered to be $n = 1$.

The optical properties of the perfused tissue layer at the red (660 nm) and infrared (940 nm) wavelengths were derived from the values presented in Table 1, using Eq. 1 and 3. For the sake of simplicity, no attempt was made to incorporate the pulsation of the arteries and arterioles in the model, since the fractional volume change of these vessels over a typical cardiac cycle is typically quite small.

Table 1. Optical properties of tissue constituents (*in unit of mm^{-1}*)

| λ (nm) | Bloodless skin dermis | | Oxygenated blood (Hct=0.45) | | Deoxygenated blood (Hct=0.45) | |
|-------------------|-----------------------|---------------------|-----------------------------|----------------------------|-------------------------------|--------------------------|
| | $\mu_{a_{dermis}}$ | $\mu'_{s_{dermis}}$ | $\mu_{a_{blood_{100\%}}}$ | $\mu'_{s_{blood_{100\%}}}$ | $\mu_{a_{blood_{0\%}}}$ | $\mu'_{s_{blood_{0\%}}}$ |
| 660 | 0.0286 | 2.2336 | 0.15 | 1.3844 | 1.64 | 1.1566 |
| 940 | 0.0245 | 0.9501 | 0.65 | 1.3187 | 0.43 | 1.1124 |

2.3 Execution of the model

The MC code was written in MATLAB® (Mathworks, Inc., USA) platform. It was initially executed to find the distribution of scattering events within perfused tissue and its variation with distance between source and detector, and with the operating wavelengths used in pulse oximetry. For this purpose, the MC code was run to simulate photon paths from the source ($r_s = 0.1mm, NA = 0.39$) to the detector ($r_d = 0.3mm, NA = 0.39$) for two fixed source-detector distances 3 mm and 6 mm, at both red and infrared wavelengths (following the method described in Section 2.1). In this fixed detector set up, a 10^4 photon

packets were detected (with total simulated photon packets $\sim 10^8 - 10^9$) for each source-detector separation at each wavelength.

MC code was executed separately for investigating the differential mean optical path (MOP) and total diffuse reflectance (W) of photons through tissue, from the circular source ($r_s = 0.05 \text{ mm}$, $NA = 0.39$) to the circular detector ($r_d = 0.05 \text{ mm}$, $NA = 0.39$) at the pulse-oximetry wavelengths (red and infrared) at different blood volumes for a range of total oxygen saturations. In this case, the detector was basically simulated as a sliding window of a width equal to the detector diameter (0.1 mm). Photon exiting from the tissue surface was detected if it had fallen within the NA of the detector fiber. Next the distance of its point of exit (on $z = 0$) from the origin was calculated from its position co-ordinates:

$$d = \sqrt{x^2 + y^2} \quad (6)$$

Meanwhile, other quantities (e.g., total optical path and remaining weight) associated with the detected photon was recorded. In this moving detector set up, a total 10^{10} photon packets were detected within a maximum source-detector spacing of 8 mm. Since pulse oximeters normally use small source-detector separations, simulations were not run further to detect photons at $d > 8$ mm to avoid excessive computation time. Also, no photons were detected below $d = 0.1$ mm, where source and detector superpose. Finally, the average optical path and weight of the photon packets detected within the sliding window of width 0.1 mm were calculated. This moving detector technique was used instead of detecting photons separately at separate fixed detector positions to save computation time.

2.4 Calculation of mean optical path and diffuse reflectance

In the MC model, the photon packet propagates through tissue with a step size (i.e., the distance between two consecutive scattering-absorption interactions) l . Each time a new step size is determined by using computer generated pseudo random number ξ ($0 < \xi < 1$) [17]. Consider a j^{th} photon packet undergoes N number of interaction events before being detected. For the i^{th} interaction, the step size is calculated as:

$$l_i = -\frac{\ln(\xi_i)}{\mu_a + \mu_s} \quad (7)$$

Therefore, the total optical path of the j^{th} photon packet is

$$OP_j = \sum_{i=1}^N l_i \quad (8)$$

For a total detected number of photons N_{ph} , the mean optical path (MOP) is calculated as:

$$MOP = \frac{1}{N_{ph}} \sum_{j=1}^{N_{ph}} OP_j \quad (9)$$

The diffuse reflectance (W) is defined as the sum of normalized statistical weights of the N_{ph} number of detected photon packets [17,25]:

$$W = \frac{1}{N_{ph} \cdot w_i} \sum_{j=1}^{N_{ph}} w_o j \quad (10)$$

where w_i and w_o are the initial (incident) and final (detected) statistical weight of j^{th} photon packet.

3. Results and discussions

Examples of the photon scatter distributions within the dermis containing 7.5% blood at a total oxygen saturation of 60%, obtained from the MC simulations (fixed detector technique), are given in figure 2. The distribution of photon packet scatters at red (660 nm) and infrared (940 nm) wavelengths are shown for $d = 3$ mm in figure 2(a) and 2(b), and for $d = 6$ mm in figure 2(d) and 2(e) respectively. From the figures it can be seen that ‘banana’ shaped distributions of optical path were obtained. As expected, the number of scattering events (N) are the highest near the source and the detector and decrease at deeper penetration depths since a smaller number of photons penetrate the tissue to greater depth. Comparative histograms of optical paths at red and infrared wavelengths at $d = 3$ mm and 6 mm are shown in figure 2(c) and 2(f) respectively. Differences in the distribution of optical paths at red and infrared wavelengths are apparent for both source-detector separations. The histograms further show the tendency of infrared photons to get accumulated in shorter optical path compared to red photons. The difference between the red and infrared optical paths are seen to increase for $d = 6$ mm compared with $d = 3$ mm. Since same number of photons were detected at both d , it is seen from the vertical axis limits of the histogram plots that the number of photons at different optical pathlengths are lesser at 6 mm than at 3 mm, which was expected.

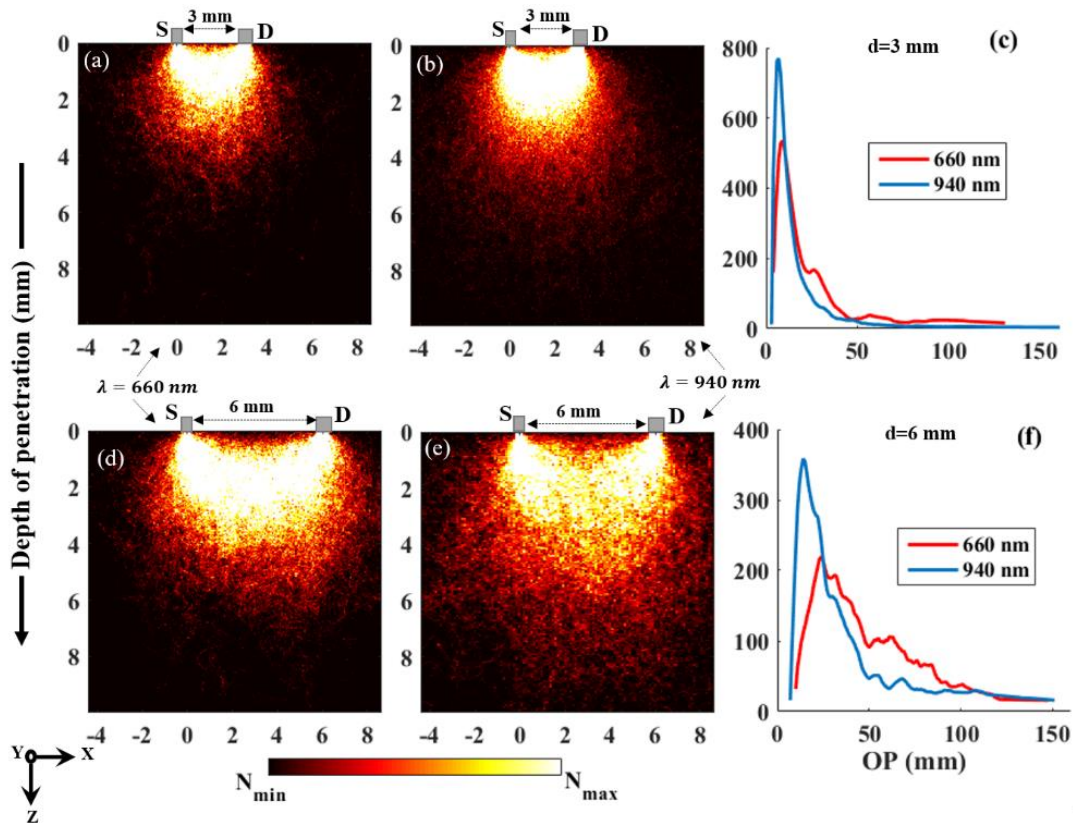


Figure 2. Distribution of optical paths in monolayer dermal skin tissue containing blood volume 7.5% at a saturation of 60% is shown at 660 nm from source (S) to detector (D), placed at a distance 3 mm (a) and at 6 mm (b); and the same at 940 nm in (d) and (e) respectively. The color bar indicates the number of scattering events (N) and each figure shows a 2-D projection of a 3-D distribution of photon packets. For comparison, all colormaps are shown within the same axis limits. The comparative histogram of the optical pathlengths of photons at two wavelengths at $d = 3$ mm and $d = 6$ mm are shown in (c) and (f) respectively.

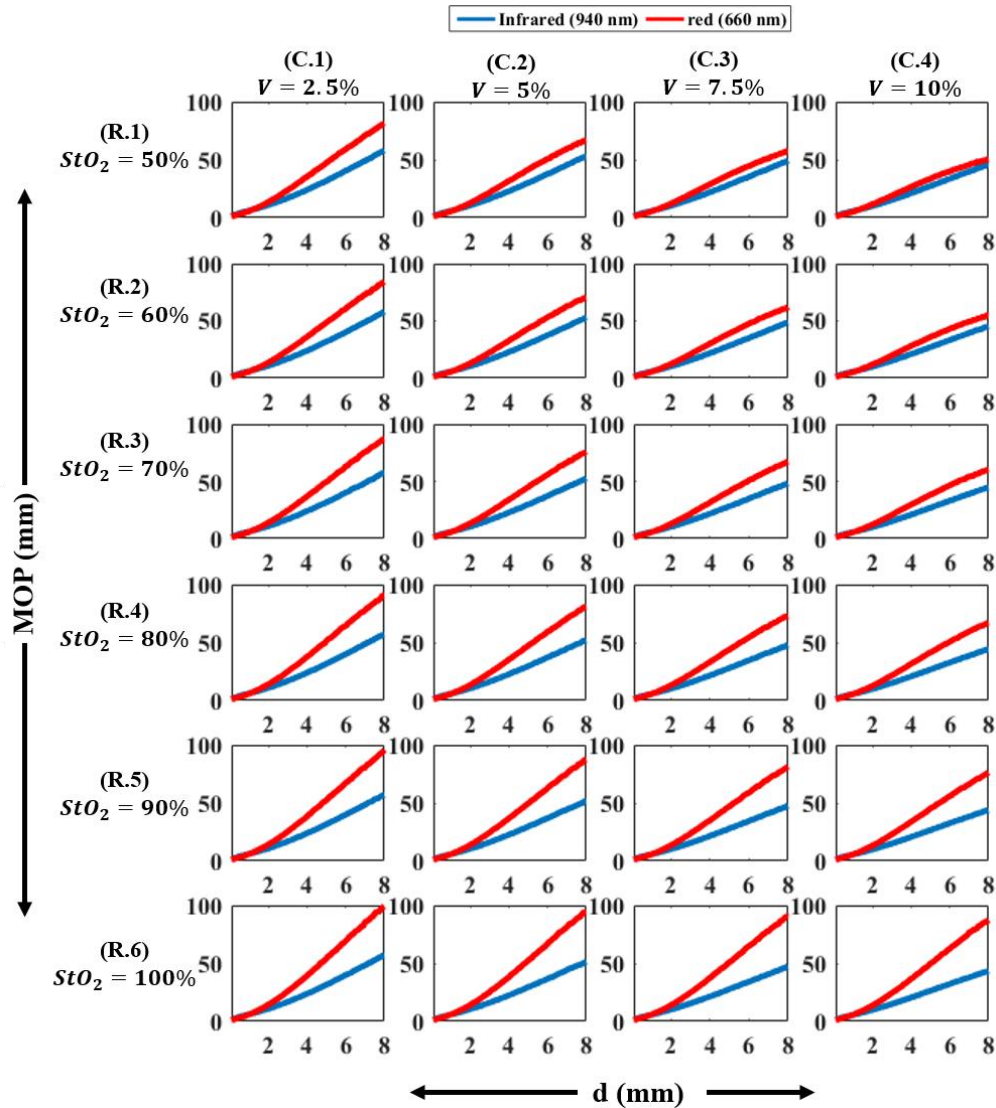


Figure 3. Differential mean optical path (*MOP*) between red and infrared wavelengths as a function of source-detector separation (*d*) for perfused dermal skin tissue is shown. Results for $StO_2 = 50\%$, 60% , 70% , 80% , 90% and 100% are presented in the rows (R.1), (R.2), (R.3), (R.4), (R.5) and (R.6) respectively. For each saturation differential mean optical path for $V = 2.5\%$, 5% , 7.5% and 10% are shown in the columns (C.1), (C.2), (C.3) and (C.4) respectively. For comparison, all graphs are plotted within the same axis limits. The red and blue lines represent *MOP* at red (660 nm) and infrared (940 nm) light respectively.

MC simulation (sliding detector technique) results exhibiting mean optical path as a function of source detector separation for skin tissue containing different blood volumes (i.e., $V = 2.5\%$, 5% , 7.5% and 10%) for a range of tissue oxygen saturations (i.e., $StO_2 = 50-100\%$ with an interval of 10%) are shown in figure 3. It is seen that photons take a longer path at the red wavelength compared to infrared in all cases. For StO_2 in the range of $50-80\%$, the difference between red and infrared optical paths tend to decrease with increasing blood volume. However, for very high StO_2 ($90-100\%$) the differences in red-infrared optical path increase with increasing blood volume. The differences in red-infrared optical path, thus, increase with blood oxygen saturation but decreases with blood volume (except at very high StO_2 , i.e., approximately 100%).

The percentage changes of the optical path between red wavelength (MOP(R)) and infrared wavelength (MOP(IR)) at a certain source-detector spacing $d = 6$ mm is illustrated in figure 4. The percentage change ΔMOP was calculated as

$$\Delta MOP = \left[\frac{MOP(R) - MOP(IR)}{MOP(IR)} \right] \times 100\% \quad (11)$$

Clearly, positive values of ΔMOP shows that MOP(R) is always greater than MOP(IR). Interestingly, ΔMOP decreases with V at lower StO_2 (50-80%) but the variation gradually decreases with higher StO_2 . For very high StO_2 (90-100%), ΔMOP increases with V .

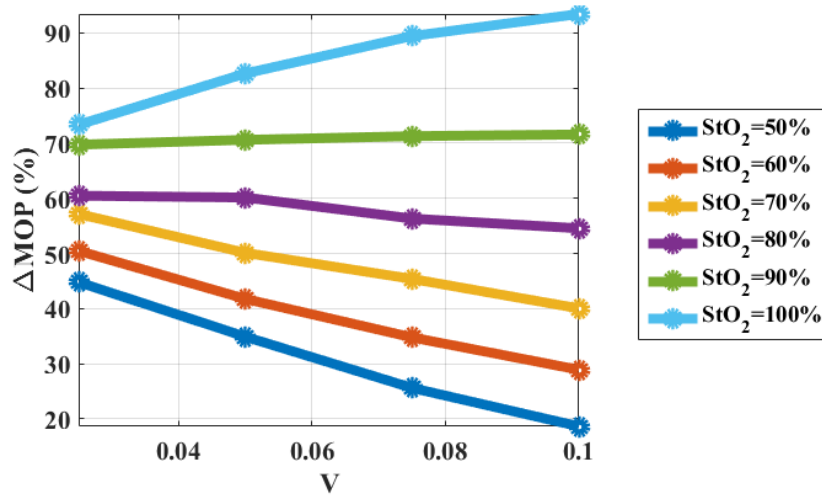


Figure 4. Percentage change in mean optical path between red and infrared light (ΔMOP), calculated for a certain source-detector separation 6 mm, as a function of blood volume (V) is shown for blood oxygen saturations $StO_2 = 50\%$, 60% , 70% , 80% , 90% and 100% . The markers represent the data points at fractional blood volume $V = 0.025$, 0.05 , 0.075 and 0.1 . ΔMOP decreases with V for lower StO_2 (~ 50 - 80%) increases with V for higher StO_2 ($\sim 100\%$).

Consider a reflectance pulse oximeter probe operating over a tissue region containing capillary blood rich in oxyhemoglobin, for example in patient breathing a high fractional concentration of oxygen ($\sim 100\%$). In this case the red photons will travel further through the tissue than the infrared photons, passing through a slightly different tissue region. The consequences of this differential optical path would be potentially greater attenuation of the red detected reflectance (PPG 'DC' signal) and since the red photons could interact with more pulsating arterioles, greater modulation of the red reflectance, i.e., increased PPG 'AC' amplitude. This effect would likely result in overestimation of the ratio of ratios and hence underestimation of arterial oxygen saturation, assuming the system was calibrated in subjects with typical oxygen saturation for air-breathing patients (i.e., around 70 - 80%). In cases of lower tissue saturation, the converse effect is likely, i.e., overestimation of arterial oxygen saturation. Due to the shape of the hemoglobin dissociation curve, however, small changes in tissue oxygen partial pressure (PO_2) result in large changes in tissue blood oxygen saturation, compared with the change in arterial oxygen saturation caused by a similar PO_2 change. As a result, inaccuracies would be expected due to any change in oxygenation, worsening at lower values of tissue PO_2 .

The Monte Carlo simulation (sliding detector technique) results for diffuse reflectance, as a function of d for different volume fractions of blood with range of oxygen saturations, are shown in figure 5.

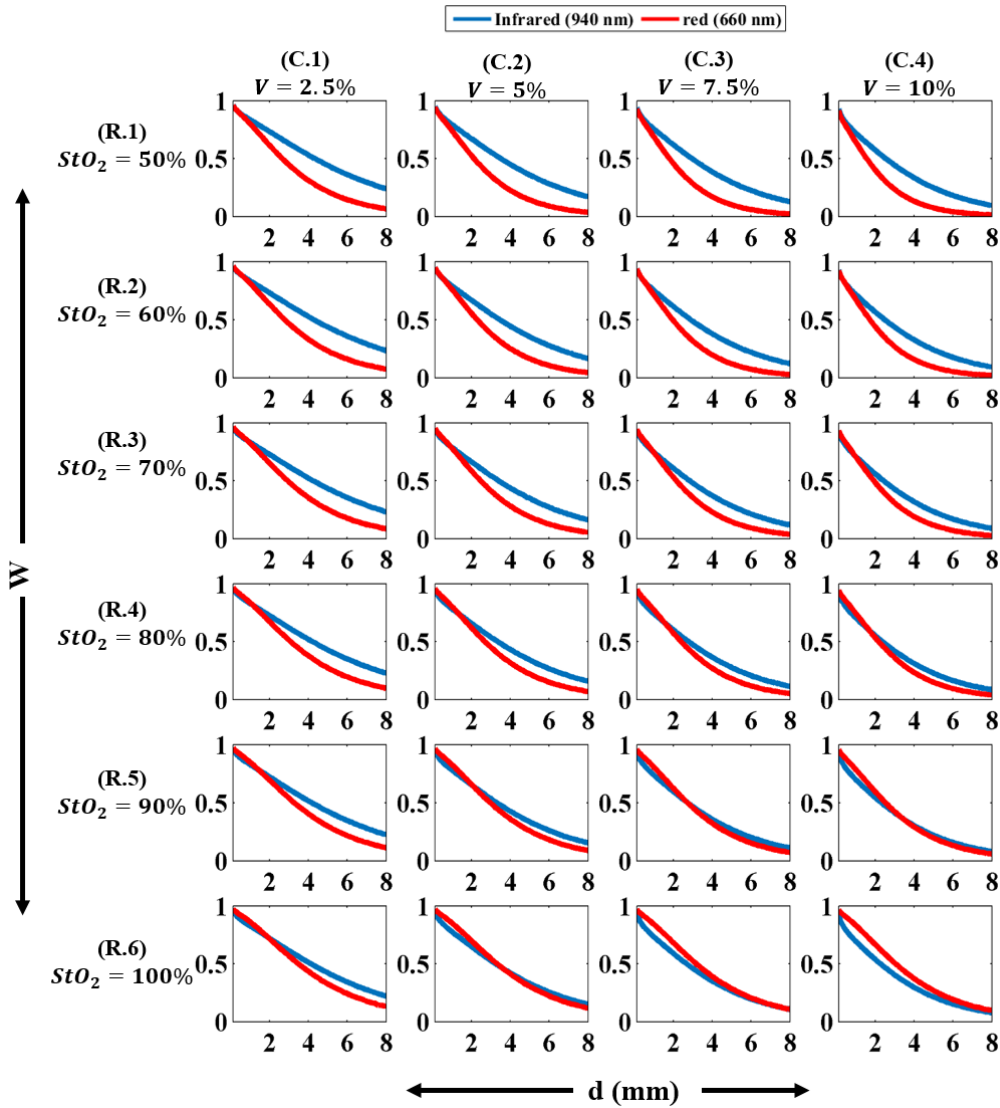


Figure 5. Differential diffuse reflectance (W) of photons between red and infrared wavelengths as a function of source-detector separation (d) for perfused dermal skin tissue is shown. Results for $StO_2 = 50\%$, 60% , 70% , 80% , 90% and 100% are presented in the rows (R.1), (R.2), (R.3), (R.4), (R.5) and (R.6) respectively. For each saturation differential mean optical path for $V = 2.5\%$, 5% , 7.5% and 10% are shown in the columns (C.1), (C.2), (C.3) and (C.4) respectively. For comparison, all graphs are plotted within the same axis limits. The red and blue lines represent W at red (660 nm) and infrared (940 nm) light respectively.

As expected, in figure 5 it is seen that W decreases with increasing source-detector separation, however the difference in the rate of decay of the reflectance between red and infrared varies according to both the blood volume and blood oxygen saturation. Results show that red light is more attenuated than infrared at oxygen saturations 50-80%, the difference in attenuation being decreased at higher blood volume. However, at very high oxygen saturations (90-100%), infrared light tends to get attenuated more than red light, which is mostly visible for high blood volumes (7.5-10%). The difference in attenuation, thus, decreases with increasing blood volume as well as increasing blood oxygen saturation. Therefore, results from figure 5 contradict some of the predictions from figure 3. This suggests that despite the increased optical path of red photons, the attenuation is largely compensated by minimal absorption of red light by

oxyhemoglobin (compared with oxyhemoglobin's stronger absorption of infrared light). This effect would minimize changes in DC intensity of the red light at higher tissue saturation, however increased modulation by arterioles leading to increased AC signal (and therefore underestimation of arterial saturation at high tissue saturations) could still occur.

Similar to Eq.11, the percentage change ΔW of the relative reflectance between red wavelength ($W(R)$) and infrared wavelength ($W(IR)$) was calculated as:

$$\Delta W = \left[\frac{W(R) - W(IR)}{W(IR)} \right] \times 100\% \quad (12)$$

The percentage changes in optical path and relative diffuse reflectance at different physiological states at a certain source-detector spacing 6 mm are presented in Table 2. Negative values of ΔW clearly show that red reflectance is lower than infrared reflectance in all cases only except very high $StO_2 \sim 100\%$ and high $V \geq 75\%$. Therefore, in low blood volume and oxygen saturation, red light is taking a longer path than infrared, thus is more attenuated, however for very high blood volume and oxygen saturation, red light is travelling further yet gets less attenuated than infrared. Therefore, different tissue volumes are 'interrogated' by light of each wavelength, and the differences depend on the tissue optical properties at different blood volume and saturation, potentially leading to erroneous reporting of SpO_2 .

Table 2. Percentage change in mean optical path (ΔMOP) and diffuse reflectance (ΔW) at different blood volumes (V) and oxygen saturations (StO_2) at $d=6$ mm.

| StO_2 | $V = 2.5\%$ | | $V = 5\%$ | | $V = 7.5\%$ | | $V = 10\%$ | |
|-------------|--------------|------------|--------------|------------|--------------|------------|--------------|------------|
| | ΔMOP | ΔW |
| 50% | +44.79% | -59.70% | +34.91% | -68.50% | +25.61% | -73.45% | +18.65% | -76.78% |
| 60% | +50.48% | -55.01% | +41.76% | -61.84% | +34.78% | -66.91% | +28.91% | -69.28% |
| 70% | +57.16% | -50.62% | +50.11% | -54.05% | +45.39% | -57.06% | +40.04% | -58.29% |
| 80% | +60.48% | -43.96% | +60.15% | -43.74% | +56.33% | -43.20% | +54.56% | -42.55% |
| 90% | +69.74% | -38.31% | +70.61% | -30.96% | +71.28% | -23.84% | +71.58% | -15.99% |
| 100% | +73.35% | -29.44% | +82.65% | -13.21% | +89.43% | +5.24% | +93.43% | +25.66% |

In figure 6, the variation of mean optical path and diffuse reflectance, as functions of d , with variable blood volume fraction at a fixed oxygen saturation 60% are shown. In both wavelengths, as shown in figure 6(a) and 6(c), MOP is reduced for higher blood volumes, which is consistent with the observations from figure 3. Vertical axis limits show that infrared pathlengths are shorter than red pathlengths. In figure 6(b) and 6(d), it is seen that the reflectance decreases considerably with increasing blood volumes at both wavelengths, with a higher attenuation visible in red compared to infrared which also agrees with the observation from figure 5.

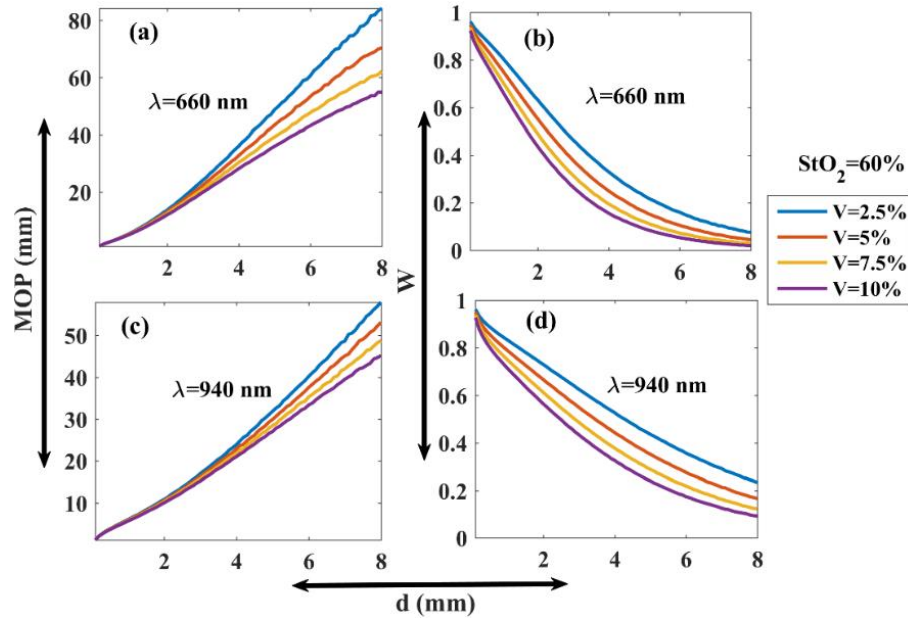


Figure 6. Mean optical path (MOP) and diffuse reflectance (W) of photon packets as functions of source-detector separation (d) are shown at a fixed $StO_2 = 60\%$ for $V = 2.5\text{-}10\%$ for $\lambda = 660 \text{ nm}$ in (a) and (b) respectively; and for $\lambda = 940 \text{ nm}$ in (c) and (d) respectively.

In figure 7, the variation of mean optical path and reflectance, as functions of d , with variable oxygen saturation fraction at a fixed blood volume 7.5% are shown. Red optical paths are shown to be increased considerably with increasing saturations, maximum MOP is at $StO_2 = 100\%$. Infrared optical paths are seen to vary slightly with varying V , however, it exhibits tendency to increase with increasing blood volume, which is the converse to red light. This also explains the results from figure 3 and 4 why ΔMOP actually increases with increasing V for $StO_2 = 100\%$. Red light is shown to be attenuated more at lower StO_2 , however, infrared attenuation changes very slightly with saturations with a maximum attenuation at 100% saturation.

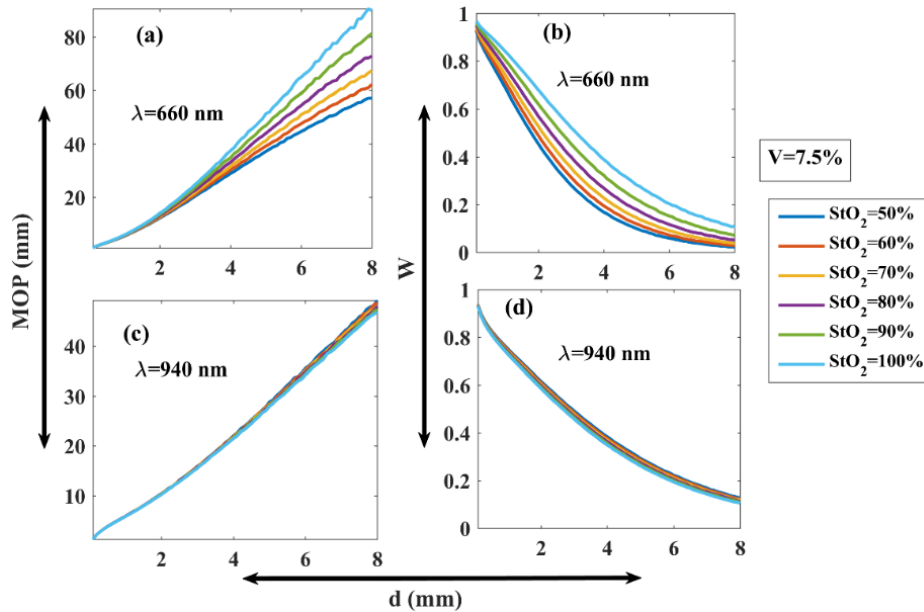


Figure 7. Mean optical path (MOP) and relative reflectance (W) of photon packets as functions of source-detector separation (d) are shown at a fixed $V = 7.5\%$ for $StO_2 = 50\text{-}100\%$ respectively for $\lambda = 660\text{ nm}$ in (a) and (b); and for $\lambda = 940\text{ nm}$ in (c) and (d) respectively.

4. Summary and Conclusion

In the present study, the distribution of optical path within perfused skin and in a typical reflectance pulse oximetry set up has been illustrated. Further to that, the dependence of the differential optical path and reflectance at red and infrared wavelengths on the volume and oxygen saturation of blood in reflectance pulse-oximetry has been demonstrated explicitly. The results presented clearly show that there is a wide range of differences in mean optical path lengths between the two wavelengths, which vary according to the blood volume and total oxygen saturation. The principle of pulse oximetry assumes that the optical paths of red and infrared light are roughly equal, i.e., the red and infrared light traverse the same region of tissue. These findings, therefore, raise concerns regarding the accuracy of pulse oximetry readings and their interpretation in the clinical setting.

The main limitations of pulse oximetry are well known and have been well documented. One of these limitations is deviation from reference measurements (e.g., blood gas analysis) at low arterial oxygen saturation values ($<70\%$). This deviation is traditionally attributed to the ethical restriction placed on most empirical studies in volunteers that subjects must not be desaturated below 70%, a requirement that results in extrapolating the calibration curve (SpO_2 vs Ratio-of-ratios) below 70%. It can be assumed that for any value of arterial SpO_2 , the saturation value of non-arterial blood, i.e., blood in the veins and capillaries, will have a much lower value than the arterial blood. From examination of the oxyhemoglobin dissociation curve [26], we may expect large differences in saturation between non-arterial and arterial blood, for example at an arterial saturation of 93-95%, a small decrease in PO_2 of 2 or 3 kPa across the capillary can result in a fall in oxygen saturation of 10% or 20%. The results presented in the paper show that this saturation value greatly affects the relative optical path length of (and hence the region of tissue ‘interrogated’ by) red and infrared light. The potential problem is worsened by the fact that most manufacturers’ empirical studies are conducted in *healthy* volunteers only. As pulse oximetry is routinely used to monitor patients with unusual physiology or pathology, differences in optical path length arising

from shifts in the hemoglobin dissociation curve, which are likely in pathological states, should be accounted for.

The combination of chosen sensor geometry and calibration function are clearly interdependent. When designing pulse oximetry sensors and algorithms, pulse oximetry manufacturers and researchers should take into account potentially large differences between red and infrared optical path length caused by variation in non-arterial blood in the tissue region beneath the probe. Adaptive calibration algorithms correcting for other measured variables (e.g., temperature, blood pH, pCO₂ etc.) would offer potential improvements to pulse oximetry accuracy during hypoxaemia.

The reflectance geometry was chosen for the simulation mainly because it could provide the model with flexibility and simplicity, showing clearly the dependence of the simulation results on the basic detector geometry, particularly the source-detector separation, which is one of the main input parameters for designing pulse oximeter. Although transmittance mode pulse oximeters are mostly used for clinical measurements, reflectance pulse oximeters also have their specific applications in cases where transmission is not possible. Example measurement sites include the forehead, wrist, arm, chest and back, while internal sites include the esophagus, mouth mucosa, trachea and rectum. Also, increasing demand for wearable PPG heart monitors has revitalized interest in reflectance pulse oximetry.

A static monolayer skin model comprising of dermis only was chosen for reasons of simplicity. Future work will incorporate additional skin layers with appropriate optical coefficients [27,28]. A fully comprehensive simulation of pulse oximetry must include arteriolar pulsation and subsequent calculation of SpO₂ from the relative amplitudes of red and infrared signals caused by this pulsation, however the present paper addresses a much more fundamental concern, i.e., the relative optical paths, penetration depth and tissue volume traversed by each wavelength (red and infrared). The differential paths described would certainly affect calculated SpO₂, however a fully comprehensive model is necessary for explicit calculation of the likely effects on the error in its reported value. Future work will consider the individual effects of (static) tissue blood and (pulsatile) arterial blood. This would require the pulsed changes in arteriolar volume to be modeled, and would provide quantitative estimation of the expected inaccuracy in reported SpO₂ imposed by different combinations of tissue saturation, blood volume, PPG signal amplitude and SpO₂.

5. Acknowledgement

The authors thank the Erasmus Mundus INTACT scholarship for funding the PhD and research program.

References

1. P. A. Kyriacou, "Pulse Oximetry in the oesophagus, Physiological Measurement", **27**(1), R1-R35 (2006).
2. P. A. Kyriacou, "Direct pulse oximetry within the esophagus, on the surface of abdominal viscera, and on free flaps", *Anesthesia and Analgesia*, **117**(4), 824-833 (2013).
3. J. T. B. Moyle, *Pulse Oximetry* (BMJ Publishing Group, 2nd edition, 2002).
4. H. Michelle, J. P. Phillips, and P. A. Kyriacou, "The effect of vascular changes on the photoplethysmographic signal at different hand elevations", *Physiological Measurement*, **36**(3), 425-440 (2015).
5. P. A. Kyriacou, D. P. Jones, R M Langford, and A J Petros, "A pilot study of neonatal and pediatric esophageal pulse oximetry", *Anesth. Analg.* **107**(3), 905-908 (2008).
6. K. Budidha and P. A. Kyriacou, "Investigation of photoplethysmography and arterial blood oxygen saturation from the ear-canal and the finger under conditions of artificially induced hypothermia", in *Proceedings of the Annual International Conference of the IEEE Engineering in Medicine and Biology Society* (EMBS, 2015), pp. 7954-7957.
7. J. M. Schmitt, "Simple photon diffusion analysis of the effects of multiple scattering on pulse oximetry", *IEEE Trans. Biomed. Eng.* **38**(12), 1194-1203 (1991).
8. P. D. Mannheim, J. Cascini, M. E. Fein, and S. L. Nierlich, "Wavelength selection for low-saturation pulse oximetry", *IEEE Trans. Biomed. Eng.* **44**(3), 148-158 (1997).

9. J. L. Reuss, "Multilayer Modeling of Reflectance Pulse Oximetry", *IEEE Trans. Biomed. Eng.* **52**(2), 153-159 (2005).
10. N. Stuban, M. Niwayama, and H. Santha, "Phantom with Pulsatile Arteries to Investigate the Influence of Blood Vessel Depth on Pulse Oximeter Signal Strength", *Sensors* **12**(1), 895-904 (2012).
11. J. L. Reuss and D. Siker, "The pulse in reflectance pulse oximetry: modeling and experimental studies", *J. Clin. Monitor. Comp.* **18**(4), 289-299 (2004).
12. A. A. Kamshilin, E. Nippolainen, I. S. Sidorov, P. V. Vasilev, N. P. Erofeev, N. P. Podolian, and R. V. Romashko, "A new look at the essence of the imaging photoplethysmography", *Sci. Rep.* **5**(5), 10494 (2015).
13. A. A. Kamshilin, O. V. Mamontov, V. T. Koval, G. A. Zayats, and R. V. Romashko, "Influence of a skin status on the light interaction with dermis", *Biomed. Opt. Express* **6**(11), 4326-4334 (2015).
14. B. C. Wilson and G. Adam, "A Monte Carlo model for the absorption and flux distributions of light in tissue", *Med. Phys.* **10**(6), 824-830 (1983).
15. S. A. Prahl, *Light transport in tissue*, thesis submitted at University of Texas Austin (1988).
16. C. Zhu and Q. Liu, "Review of Monte Carlo modeling of light transport in tissues", *J. Biomed. Opt.* **18**(5), 050902 (2013).
17. L. Wang, S. L. Jacques, and L. Zheng, "MCML- Monte Carlo modeling of light transport in multi-layered tissues", *Comput. Meth. Prog. Bio.* **47**(2), 131-146 (1995).
18. J. P. Phillips, P. A. Kyriacou, and D. P. Jones, "Calculation of Photon Path Changes due to Scatter in Monte Carlo Simulations", in *Proceedings of the Annual International Conference of the IEEE Engineering in Medicine and Biology Society* (EMBS, 2010), pp. 4959-4962.
19. A. J. Welch and M. J. C. van Gemert eds, *Optical-Thermal Responses of Laser-Irradiated Tissue* (Springer, 2nd edition, 2009), Chap. 5.
20. J. P. Phillips, *New optical methods for the measurement of oxygen saturation in cerebral tissue*, thesis submitted at Barts and Queen Mary, University of London (2009).
21. S. L. Jacques, "Skin Optics", <http://omlc.org/news/jan98/skinoptics.html>.
22. R. Simpson, J. Laufer, M. Kohl, M. Essenpreis, and M. Cope, "Skin Optical Properties: Caucasian dermis optical properties (epidermis and dermis)" dataset, <http://www.ucl.ac.uk/medphys/research/borl/intro/skin>.
23. N. Bosschaart, G. J. Edelman, M. C. G. Aalders, T. G. van Leeuwen, and D. J. Faber, "A literature review and novel theoretical approach on the optical properties of whole blood", *Lasers Med. Sci.* **29**(2), 453-479 (2014).
24. J. M. Steinke and A. P. Shepherd, "Diffusion model of the optical absorbance of whole blood", *J. Opt. Soc. Am. A* **5**(6), 813-822 (1988).
25. I. Meglinski and S. J. Matcher, "Computer simulation of the skin reflectance spectra", *Comput. Meth. Prog. Bio.* **70**(2), 179-186 (2003).
26. J.B. West, *Respiratory Physiology: The Essentials* (Lippincott Williams & Wilkins, 2012), Chap. 6.
27. I. Meglinski and S. J. Matcher, "Quantitative assessment of skin layers absorption and skin reflectance spectra simulation in the visible and near-infrared spectral regions", *Physiol. Meas.* **23**(4), 741-753 (2002).
28. P. Zakharov, M S Talary and A Caduff, "A Wearable Diffuse Reflectance Sensor For Continuous Monitoring Of Cutaneous Blood Content", *Physiol. Meas.* **54**(17), 5301 (2009).